

Predicting Transport in Lyotropic Liquid Crystal Membranes with Molecular Dynamics Simulations

Michael R. Shirts

August 17, 2017

Introduction

Nanostructured membrane materials have become increasingly popular for aqueous separations applications such as desalination and biorefinement because they offer the ability to control membrane architecture at the atomic scale allowing the design of solute-specific separation membranes [1]. Most membrane-based aqueous separations of small molecules can be achieved using reverse osmosis (RO) or nanofiltration (NF) [2].

While RO and NF have seen many advances in the past few decades, they are far from perfect separation technologies. Current state-of-the-art RO membranes are unstructured with tortuous and polydisperse diffusion pathways which leads to inconsistent performance [3]. Necessarily high feed pressures drive up energy requirements which strain developing regions and contribute strongly to CO₂ emissions [4]. Moreover, designing RO membranes to achieve targeted separations of specific solutes is nearly impossible because various solutes dissolve into and diffuse through the polymer matrix at different rates [5]. At best, one can exploit these differences to create a functional selective barrier. NF was introduced as an intermediate between RO and ultrafiltration, having the ability to separate organic matter and salts on the order of one nanometer in size. Larger and well-defined pores drive down energy requirements while still affording separation of solutes as small as ions to some degree [2]. This is why NF is often used as a precursor to reverse osmosis. Unfortunately, NF membranes, like RO, are produced with a pore size distribution which limits their ability to perform precise separations [6].

Nanostructured membranes can bypass many of the performance issues which plague traditional NF and RO membranes. One can accomplish targeted separations by tuning size and functionality of the molecular building blocks which form these materials. Solute rejecting pores can have their size tuned uniformly, resulting in sharp size cut-offs. Entirely different mechanisms may govern transport in a given nanostructured material which can inspire novel separation techniques.

Development of nanostructured materials has been limited by the ability to synthesize and scale various fundamentally sound technologies. Graphene sheets are atomically thick which results in excellent permeability but defects during manufacturing severely impact selectivity [7]. Molecular dynamics simulations of carbon nanotubes show promise [1] but synthetic techniques are unable to achieve scalable alignment and pore monodispersity [8, 9]. Zeolites have sub-nm pores with a narrow pore size distribution and MD simulations exhibit complete rejection of solvated ions [10], however, experimental rejection was low and attributed to interstitial defects formed during membrane synthesis [11].

Self assembling lyotropic liquid crystals (LLCs) are a suitable candidate for aqueous separation applications. They share the characteristic ability of nanostructured membrane materials to create highly ordered structures with the added benefits of low cost and synthetic techniques feasible for large scale production [12]. LLCs are versatile and controllable with a large chemical design space available for membrane design. We will be studying assemblies formed by Na-GA3C11 (Fig 1a), a system which has been extensively studied experimentally [13, 14, 15, 12, 16]. Neat monomer forms the thermotropic, Col_h phase. The presence of small amounts of water results in the H_{II} phase. In both cases, monomers assemble into mesophases made of hexagonally packed, uniform size, cylinders with hydrophilic groups oriented inward towards the pore center and hydrophobic groups facing outward. Until recently, the mesophases could not be macroscopically aligned, resulting in a low flux membrane, slowing research in the field. In 2014, Feng et al. showed that the mesophases could be aligned using a magnetic field with subsequent crosslinking to lock the structure

in place [12]. In 2016, Feng et al. showed that the same result could be obtained using a technique termed soft confinement [16]. Following this breakthrough, research into LLC membranes has been reinvigorated. We have chosen to focus our initial efforts on the development of a model of the Col_h phase membrane in order to accelerate development of LLC membranes. Compared to the H_{II} phase, the Col_h phase is a simpler starting point, due to the absence of water, and has equivalent experimental structural data. .

A molecular level understanding of LLC membrane structure will elucidate small molecule transport mechanisms, providing guidelines for reducing the chemical space for the design of monomers used to create separation-specific membranes. We do not yet understand how to reduce the effective pore size or how to tune the chemical environment in the nanopores for effective water desalination and small organic separations. Rejection studies show that this membrane can not perform separations of solutes less than 1.2 nm because the pores are too large [14]. Over the past 20 years, LLC membrane studies have been limited primarily to Na-GA3C11 with some characterization done after minor structural modifications [17]. Optimization has been performed through trial and error. The only source of predictive modeling has been macroscopic models which likely do not adequately describe transport at these length scales. A good model should incorporate a detailed picture of the nanoscopic pore structure. Pore components may play a role in the rejection of charged or uncharged solutes. Choice of counterion may influence the establishment of a Donnan potential affecting the degree to which the membrane can exclude charged species. Moieties inside the pores may interact with neutral solutes, rejecting on the basis of shape and size, rather than just hydrodynamic radius. An atomistic understanding of pore structure and its influence on transport can help identify performance bottle necks and direct design of future membranes.

A clear picture of the nanoscopic structure of LLC membranes, gained by building a molecular model will provide evidence to support or call into question past drawn conclusions that have largely guided our understanding of the system. A clear picture of the nanoscopic LLC membrane structure, gained by building a molecular model will provide evidence to answer existing and newly proposed questions. The arrangement of monomers in the channels is thought to be confined to the pore walls. It is possible they are arranged more randomly. This would change the way one thinks about molecules diffusing through the membrane. The Col_h phase is described as having pores made of disks or layers stacked on top of one another, each containing a set number of monomers. A simple simulation study of a similar molecule suggests that there are 4 monomers in each disk [18]. A separate calculation based on the volume of the liquid crystal monomers proposes that there are seven monomers in each layer [17]. Once we know the number of monomers in each layer, we still do not know how monomers in each layer are positioned with respect to other layers. One of the driving forces for self assembly in this system is thought to be pi-pi stacking interactions between aromatic headgroups [19]. Gas phase ab initio studies of benzene dimers have shown a clear energetic advantage for parallel displaced and T-shaped pi-pi stacking conformations versus a sandwiched conformation [20]. Substituted benzene rings exhibit an even stronger pi-pi stacking attraction which favors the parallel displaced configuration in all cases except where the substitutions are extremely electron withdrawing [21, 22]. While we might be able to provide answers to these questions using a molecular model, there remains the possibility that there is more than one metastable state associated with a given LLC system. We must be able to identify which states can be produced experimentally and what implications each state might have regarding transport properties.

We must show that the developed molecular model is consistent with physical observations so that we can rely on conclusions drawn about structural features characteristic of the system. This article will illustrate the development of a predictive molecular model and the steps taken to ensure it mimics the real system within the constraints inherent to MD. To understand how physically realistic the model is, validation by comparison to experiment is necessary. We are primarily interested in reproducing the conclusions about structure which have been made from XRD experiments and ionic conductivity measurements [16]. We have compared simulated X-ray diffraction patterns to experiment in order to match major features present in the 2D patterns. We calculate ionic conductivity using two agreeing methods. We examined the the influence of crosslinking on membrane structure. The analysis used in this paper can be readily extended to the H_{II} phase and other similar LC systems.

Methods

HII monomers were parameterized using the Generalized AMBER Forcefield [23] with the Antechamber package [24] provided with AmberTools16 [25]. Atomic charges were assigned using tools from Openeye Scientific Software. All molecular dynamics simulations were run using the latest version of Gromacs 2016. [26, 27, 28, 29]

An ensemble of characteristic, low-energy vacuum monomer configurations were constructed by applying a simulated annealing process to a parameterized monomer. Monomers were cooled from 1000K to 50K over 10 nanoseconds. A low energy configuration was pulled from the trajectory and charges were reassigned using the am1bccsym method of molcharge shipped with Openeye Scientific software's QUACPAC. Using the new charges, the monomer system was annealed again and monomer configurations were pulled from the trajectory to be used for full system construction (Figure 1a).

The timescale for self assembly of monomers into the hexagonal phase is unknown and likely outside of a reasonable length for an atomistic simulation, calling for a more efficient way to build the system. Previous work has shown a coarse grain model self assemble into the H_{II} phase configuration in \approx 1000 ns [30]. Atomistic self-assembly was attempted by packing monomers into a box using Packmol [31]. Simulations of greater than 100 ns show no indicators of progress towards an ordered system. To bypass the slow self-assembly process, python scripts are used to assemble monomers into a structure close to the expected equilibrium configuration (Figure 1). A short, restrained equilibration, followed by NPT simulations between 400 and 500 ns, allows the initial configuration to relax into an equilibrium configuration. Our logic for choosing a starting configuration and the details of the equilibration schemes are presented below.

A typical simulation volume contains four pores in a monoclinic unit cell, the smallest unit cell that maintains hexagonal symmetry when extended periodically. Each pore is made of twenty stacked monomer layers with periodic continuity in all directions, avoiding any edge effects and creating an infinite length pore ideal for studying transport. A small number of layers is preferred in order to reduce computational cost and to allow us to look at longer timescales. Ultimately, we chose to build a system with 20 monomer layers in each pore in order to give sufficient resolution when simulating X-ray diffraction patterns.

Initial guesses for the remaining structural parameters were chosen based on experimental data and treated as variables during model development. The distance between pores was based on experimental SAXS data for this system [16]. Initial configuration pore spacing was chosen to be 10 % larger than the experimental value to reduce unintended repulsions resulting from a tightly packed initial configuration. The layer spacing was based on experimental 2D WAXS data which shows reflections corresponding to features spaced 3.7 Å apart. It has been hypothesized that the features are present due to pi-pi interactions between stacked aromatic rings [12]. Our simulations tend to equilibrate to a wider interlayer spacing of \approx 4.1 Å, which inspired separate systems starting with layer spacings greater than 4 Å. Initial pore radius estimates of 0.6 nm were based on past TEM images and size exclusion rejection data[12, 16, 14]. The relative interlayer orientation was chosen based on clues from diffraction data as well as the various known stacking modes of benzene and substituted benzene rings: sandwiched, parallel-displaced and T-shaped (Figures 2a to 2c). The T-shaped configuration was ruled out based on the inconsistency of its \approx 5 Å equilibrium stacking distance. The system's preference towards the sandwiched vs. parallel displaced stacking modes was left to be explored. Visualization of each configuration (Figures 2d and 2e) suggests entropic differences based on the way the tails are able to pack. This difference may explain, in part, which stacking mode is more favorable.

An equilibration scheme with position restraints placed on aromatic rings prevents unrealistic jumps during early equilibration steps. Restraints fix monomer head groups in the sandwiched or parallel-displaced configurations while allowing monomer tails to settle. Doing so also mitigates system dependence on initial monomer configuration. Restrained equilibrations are run in the NVT ensemble. Every 50 ps, force constants are reduced by the square root of its previous value, starting from 1e6 KJ mol⁻¹ nm⁻². Once the force constant is below 10 KJ mol⁻¹ nm⁻², the restraints are slowly released until there is no more restraining potential. The resulting unrestrained structure is allowed to equilibrate in the NPT ensemble for 400 - 500 ns.

Using an equilibrated structure, a crosslinking procedure was performed in order to better parallel synthetic procedures. The purpose of crosslinking is to maintain macroscopic alignment of the crystalline domains, ensuring aligned, hexagonally packed pores. For that reason, we are not concerned with replicating the kinetics of the reaction, but instead emphasize the consistency of the final structure with experimental

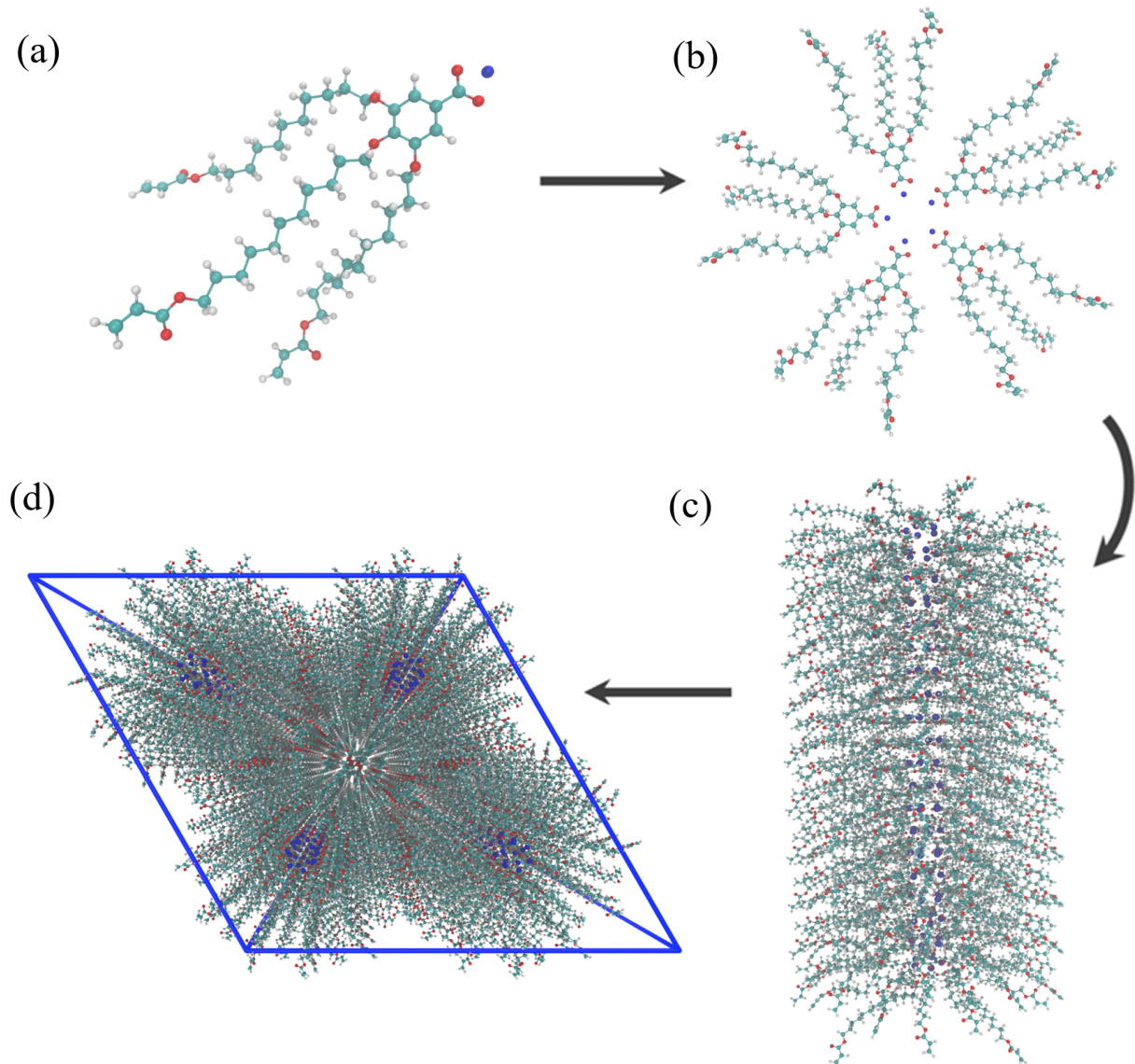
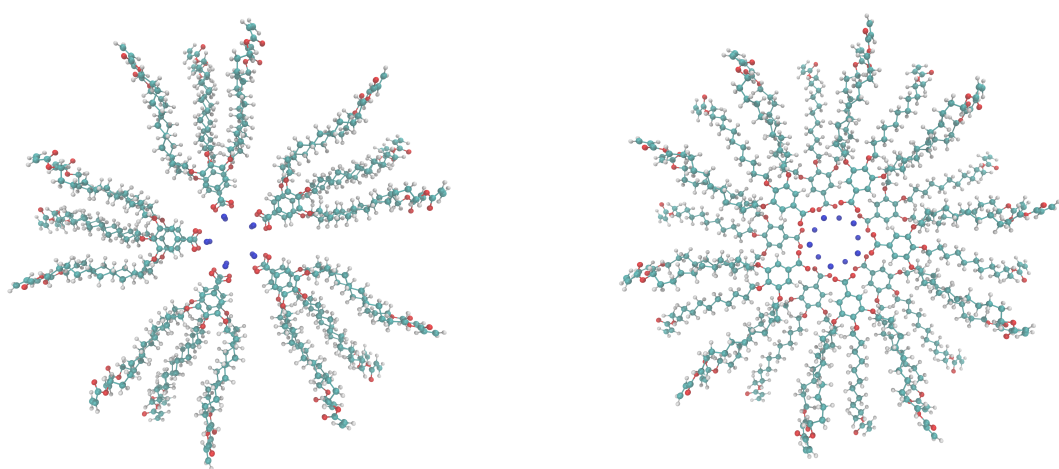
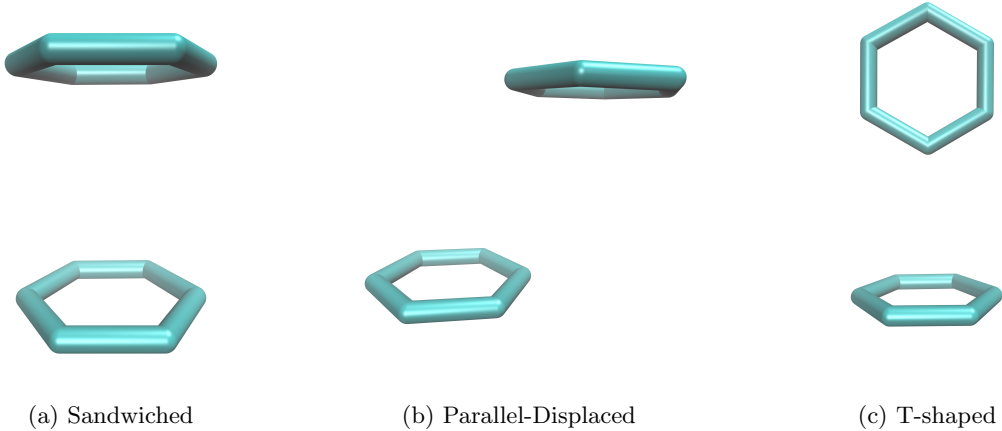


Figure 1: (a) Single monomers are parameterized and annealed to produce a low energy configuration. (b) Monomers are rotated and assembled into layers with hydrophilic centers. (c) Twenty layers are stacked on top of each other to create a pore. (d) Pores are duplicated and place in a monoclinic unit cell



(d) Two monomer layers stacked in the sandwiched configuration (e) Two monomer layers stacked in the parallel-displaced configuration

Figure 2

structural data. The algorithm was developed based on the known reaction mechanism. Crosslinking of this system is a free radical polymerization (FRP) taking place between terminal vinyl groups present on each of the three monomer tails. FRPs require an initiator which bonds to the system, meaning new atoms were introduced into the system. For simplicity, the initiator was simulated as hydrogen and made present in the simulation by including them in all possible bonding positions as dummy atoms. The crosslinking procedure is carried out iteratively. During each iteration, bonding carbon atoms are chosen based on a distance cut-off. The topology is updated with new bonds and dummy hydrogen atoms are changed to appropriate hydrogen types. Head-to-tail addition was the only propagation mode considered due to its dominance in real systems. Direction of attack was not considered because the resultant mixture is racemic. The resulting crosslinked structure has an even distribution of crosslinks between monomer tails of the same monomer, monomers stacked on top of each other and monomers in other pores, including across periodic boundaries. The pore spacing shrinks by $\approx 1 \text{ \AA}$ and stays constant under a range of simulation conditions.

Simulated X-ray diffraction patterns were generated based on atomic coordinates to give a deeper understanding of the pore structure and spacing. All atomic coordinates were simulated as gaussian spheres of electron density corresponding to each atom's atomic number. A three dimensional fourier transform (FT) of the array of electron density results in a 3 dimensional structure factor representing the unit cell in reciprocal space. We perform an angular average of the structure factor about the z axis to generate a 2D cross section close to what one would see experimentally. We matched experimental 2D WAXS patterns by iterative improvement of our choice of initial structure and equilibration procedure.

Ionic conductivity was calculated using two different methods for robustness. The Nernst-Einstein relation relates the DC ionic conductivity to ion diffusivity, D , concentration, C , ion charge, q , the boltzmann constant, k_b , and temperature, T :

$$\sigma = \frac{q^2 C D}{k_b T}$$

Sodium ion diffusion coefficients were found by calculating the slope of the linear region of the mean square displacement curve as indicated by the einstein relation [32]. Ion concentration was measured with respect to the entire unit cell. The second method, termed the 'Collective Diffusion' model [33], measures the movement of the collective variable, Q , which is defined as the amount of charge transfer through the system. The diffusion coefficient of Q , D_Q , can be calculated using the einstein relation. The conductance, γ of the system can be calculated as:

$$\gamma = \frac{D_Q}{k_b T}$$

Conversion to ionic conductivity is achieved by multiplying by channel length and dividing by the membrane cross sectional area. A full derivation of the model can be accessed elsewhere [33].

Results and Discussion

Determination of system structural details

In order to construct an initial configuration which gives reliable trends, we need to understand the composition of layers, how far apart to stack the layers, and how to orient them with respect to each other. To verify our choices for each parameter, we compare our calculations to experimental small angle X-ray scattering (SAXS), wide angle X-ray scattering (WAXS), and ionic conductivity measurements.

To discern the composition of the monomer layers, we ran simulations of systems created with 4 - 8 monomers per layer. Both the sandwiched and parallel displaced configurations were tested. All systems remained stable for at least 50 ns. Pore spacings were calculated by measuring the distance between the pore centers. Pore centers were located by averaging the coordinates of sodium ions in their respective pores. Statistics were generated using the bootstrapping technique. Table 1 shows the pore spacing for all systems tested. Systems built with 5 monomers in each layer equilibrate to a pore spacing that is most consistent with the experimental value of 4.12 nm derived from SAXS measurements (Figure 4b). The remainder of this discussion will focus on the analysis of systems built with 5 monomers per layer. Pair correlation functions calculated between aromatic rings along the length of the pores indicate that systems prefer to stay partitioned into layers (Fig 3).

Monomers per layer	Starting Configuration	
	Sandwiched	Parallel Displaced
4	3.71 ± 0.08	3.82 ± 0.06
5	3.99 ± 0.08	4.16 ± 0.09
6	4.83 ± 0.08	4.85 ± 0.05
7	4.73 ± 0.06	4.84 ± 0.06
8	5.08 ± 0.08	5.46 ± 0.07

Table 1: The pore spacing of the model increases as number of monomers in each layer increases. The pore spacing of a system starting in the sandwiched configuration is systematically lower than that started in an offset configuration. Systems built with 5 monomers per layer in a parallel displaced configuration results in a pore spacing closest to experimental data

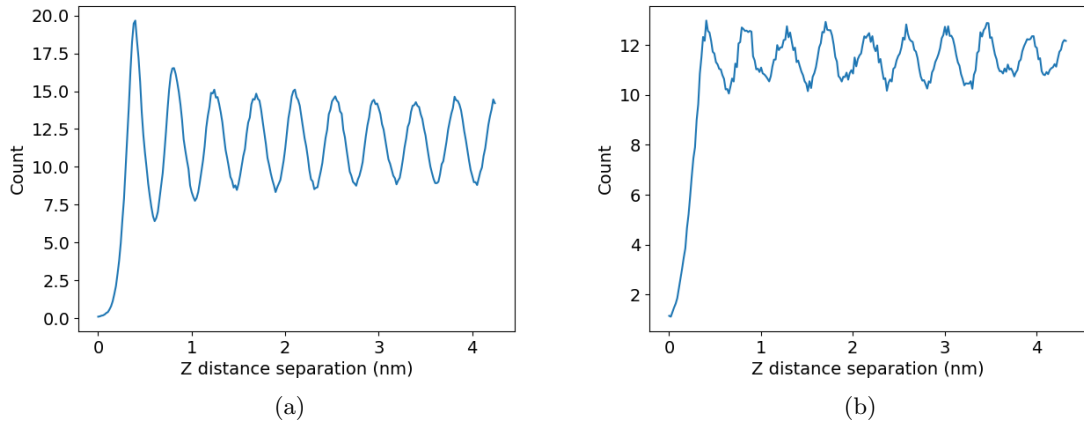


Figure 3: Pair distribution functions of aromatic carbons for the (a) 5 monomer per layer, sandwiched and (b) 5 monomer per layer, parallel displaced configurations. Spikes in the distribution mark distinct layers. The magnitude of the spikes with respect to the average suggest that the 5 monomer per layer, sandwiched configuration possesses the highest degree of layer partitioning.

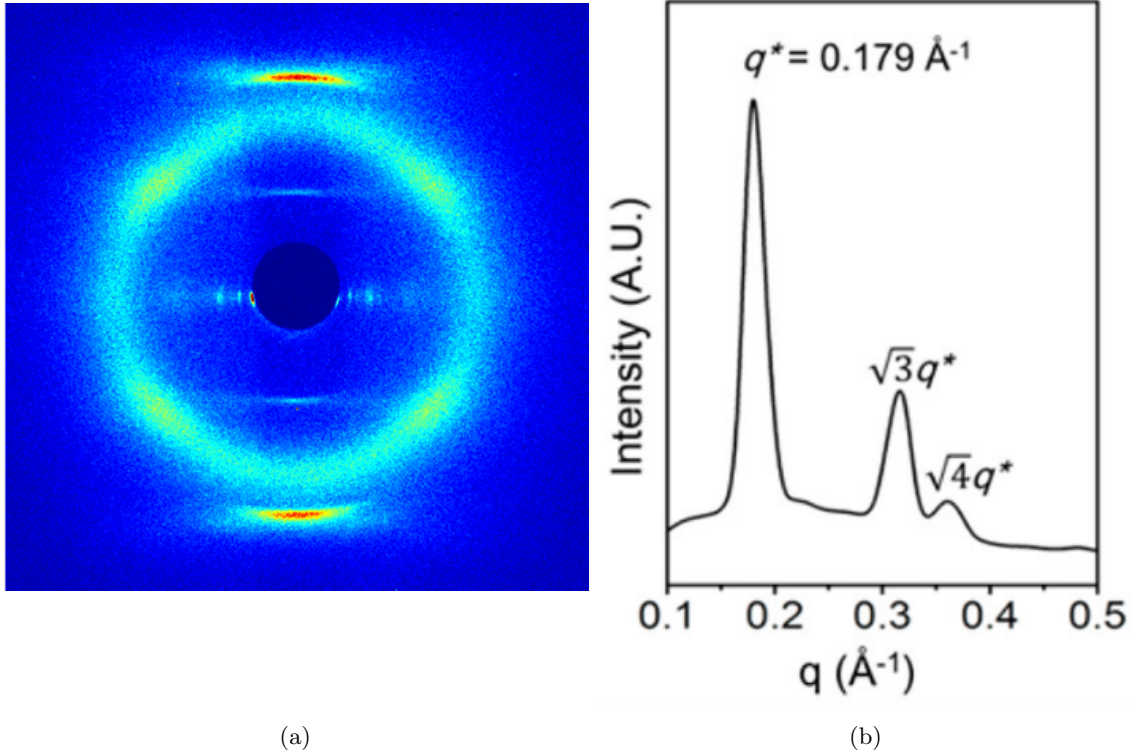


Figure 4: (a) 2D wide angle X-ray scattering gives details about repeating features less than 1 nanometer apart. (b) 1D small angle X-ray scattering indicates hexagonal packing of pores as well as the spacing between pores.

Experimental WAXS measurements encode all structural details. There are five major features present in the 2D experimental pattern which our model intends to reproduce (Figure 4a). The first is located at $q_z = 1.7 \text{ \AA}^{-1}$, corresponding to a real spacing of 3.7 \AA . The reflection is attributed to pi-pi stacking between aromatic rings in the direction perpendicular to the membrane plane, or z-axis. For simplicity, this reflection will be referred to as R-pi. A weak intensity line is located at exactly half the q_z value of R-pi ($q_z = 0.85 \text{ \AA}^{-1}$), corresponding to a real space periodic spacing of 7.4 \AA . This reflection has been interpreted as 2_1 helical ordering of aromatic rings along the z axis and will therefore be referred to as R-helix. If positions of the aromatic rings can be traced by a helix, then for each turn in the helix, there should be two aromatic rings. A third major reflection is marked by a low intensity ring located at $r = 1.4 \text{ \AA}^{-1}$. The real space separation corresponds to 4.5 \AA which is characteristic of the average spacing between packed alkane chains. This reflection will be called R-alkanes. Within R-alkanes, are four spots of higher intensity which will be called R-spots. All are located ≈ 40 degrees from the q_z axis in their respective quadrants. In many liquid crystal systems this can be explained by the tilt angle of the alkane chains with respect to the xy plane. The final major reflections correspond to the spacing and symmetry of the d_{100} plane which can be related to the distance between pores. The feature, which will be called R-pores, is characterized by dots along $q_z = 0$. The spacing between dots is indicative of the hexagonal symmetry of the packed pores. It is easiest to interpret the data by radially integrating the 2D data to get a 1D curve which is shown in Figure 4b.

The initial distance between layers can influence the approach towards equilibrium. Equilibrated systems built according to the 3.7 \AA spacing indicated by R-pi are characterized by a defined, cylindrical and open pore structure. Aromatic rings are arranged in a helical conformation. We will refer to this system as Basin A (Figure 5a). Simulations of systems built with layers stacked greater than 4 \AA apart results in a pore structure characterized by high radial disorder, while still maintaining partitioning between hydrophobic and hydrophilic regions. This will be called Basin B (Figure 5b). It is apparent that this LLC membrane may exist in at least two metastable states. The distinct difference in pore structure exhibited by each phase will

likely lead to different transport mechanisms. Understanding which phase exists experimentally is necessary in order to appropriately study the system.

Basin A and Basin B are two configurationally metastable basins. We hesitate to classify the basins as separate phases. We hypothesize that Basin B is present at higher temperatures. This is evidenced by a simulation of a system in Basin A whose temperature was linearly ramped from 280K to 340K over 100 ns. Visually, there is a distinct change in pore structure from one characteristic of Basin A (Figure 5a) to one characteristic of Basin B (Figure 5b). To quantify our observation, we chose three easily measurable order parameters: the distance between pores, the membrane thickness and the ratio of pore radius to the uncertainty in pore radius. The distance between pores was measured as described previously. The membrane thickness was measured using the length of the z box vector. The pore radius was measured by calculating the distance between the center of mass of each aromatic ring and the center of mass of all aromatic rings in their respective pores. The pore radius is divided by its uncertainty in order to understand the degree to which monomers obstruct the pore region. Referring back to our temperature ramped system, the slope of all order parameters change around 315K - 325K (Figures 5c to 5e) indicating the possibility of an abrupt change in system ordering. To prove that the basins are in fact two different phases, we must observe evidence of a first order phase transition, which would be marked by a discontinuity in an order parameter as a function of temperature. Our 100 ns temperature ramp may have been too fast causing the system to suffer from hysteresis. To mitigate hysteresis, we performed a slow, stepwise temperature ramp. Starting from structures equilibrated at 280K, the system temperature was raised to 300K and allowed to equilibrate for 200 ns. At the end of 200 ns, the temperature was raised 5K and equilibrated again for 200 ns. We repeated this process until the system was equilibrated for 200 ns at 320K. In all cases, we observed smooth changes in order parameters as temperature was increased implying that we can not yet claim the existence of two phases (Figure 6). The same process will continue to be repeated up to 340K in the near future since we have not surpassed the temperatures where we observe abrupt slope changes in pore spacing and membrane thickness (Figures 5c and 5d).

We varied the relative interlayer orientation between sandwiched and parallel-displaced based on our knowledge of the stability of these two pi-stacking modes. Short NVT simulations were run with position restraints on aromatic ring carbon atoms. Simulated X-ray diffraction patterns generated from each configuration establish a difference between the two stacking modes (Figure 7). In each pattern, R-alkanes is present at a distance of $\approx 1.5 \text{ \AA}^{-1}$. R-pi is also present in each pattern, although it appears to intersect R-alkanes because the spacing between aromatic rings is similar to the alkane chain packing. The difference in aromatic ring spacing between experiment and simulation is likely a result of the inability of GAFF to properly handle aromatic interactions. The sandwiched configuration shows R-spots in the expected location. A faint reflection is present in the location of R-helix. The parallel displaced configuration contains two lines of high intensity with maximum intensity occurring where they intersect the alkane chain region due to constructive interference between the two features. The lines are located where one would expect to see R-helix and, perhaps coincidentally, the intersection with R-alkanes occurs where one would expect to see R-spots. As the simulation is progressed, the full line begins to fade (Figure 8). Most significantly, the line is no longer present where R-helix exists.

Full comparison of experimental 2D WAXS with simulated X-ray diffraction patterns produced from equilibrated MD trajectories shows the most consistency with the sandwiched configuration in Basin A. Systems were built in both the parallel displaced and sandwiched configurations with an intial layer spacing of 3.7 \AA . A third system was created by stacking layers in the sandwiched configuration 5 \AA apart in order to guide it towards Basin B. For ease of reference, the third system will be referred to as the disordered system. The three systems were equilibrated according to our procedure with NPT simulations of greater than 400 ns. Simulated diffraction patterns were generated using portions of the trajectory after equilibration. Equilibration was detected when the distance between pores and the membrane thickness stopped changing. Simulated diffraction patterns for all three structures are shown in Figure 8. The equilibrated parallel displaced structure exhibits R-alkanes and R-pores in the expected locations. Due to low resolution, making out the individual spots of R-pores is challenging and can be validated upon full spherical integration of the 3D structure factor. However, the same information can be extracted by measuring the pore spacing as described earlier. R-pi is also present, intersecting R-alkanes at a lower q value than in experiment. The rings prefer to stack $\approx 4.1 \text{\AA}$ apart as opposed to 3.7 \AA . R-helix and R-spots are also both missing. The line which intersected both of these features in the restrained simulations faded upon equilibration which

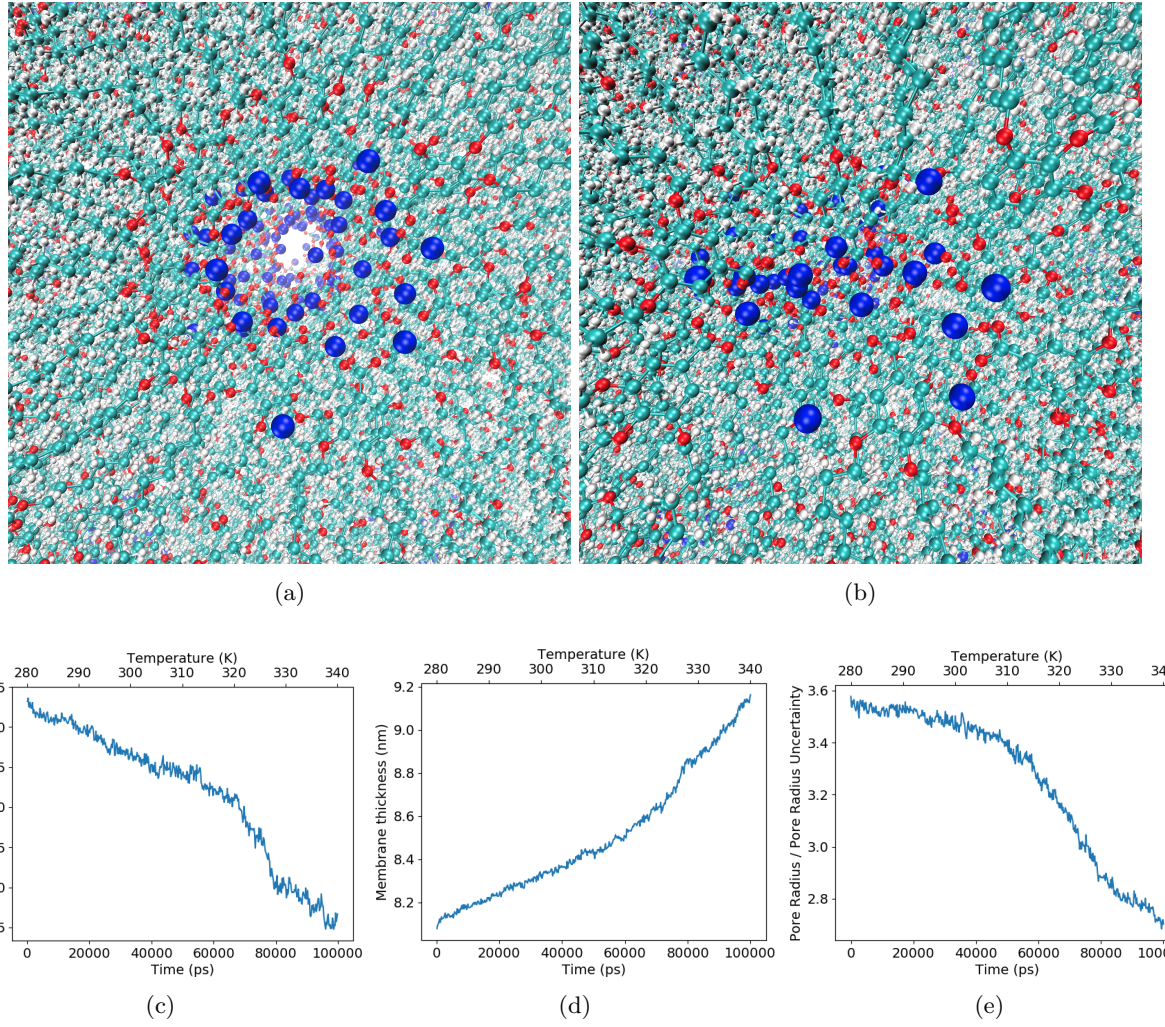


Figure 5: (a) The open pore structure exhibited by a structure equilibrated at 280K is characteristic of Basin A. (b) The closed pore structure with a high degree of radial disorder exhibited when the structure in (a) is heated to 340K is characteristic of Basin B. (c) A plot of distance between pores vs. temperature changes slope near 325K. (d) A plot of membrane thickness vs. temperature changes slope near 325K. (e) The plot of the ratio of pore radius to its uncertainty changes slope near 315K.

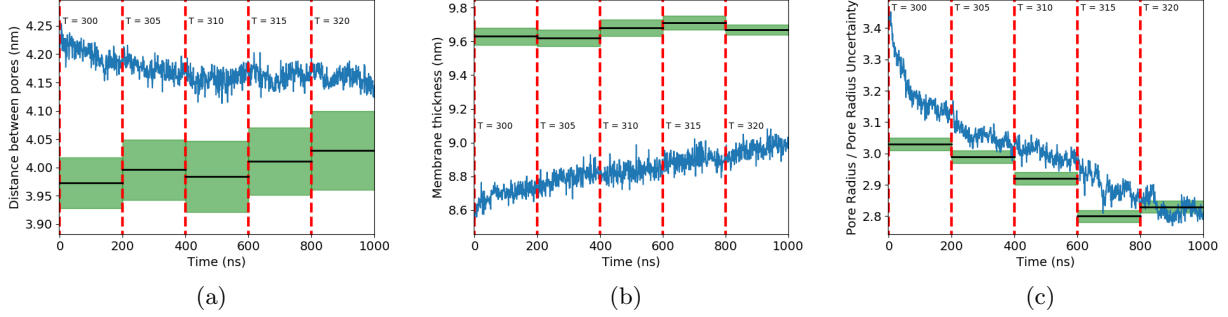


Figure 6: In all cases, blue lines represent the measured value of the order parameter, black lines are average values calculated from equilibrated Basin B systems at each temperature, green shaded regions represent the standard deviation of each of the black line values, and red dashed lines show where the temperature is bumped to the next level. (a) The pore spacing decreases smoothly as it approaches Basin B values. (b) Membrane thickness increases steadily with temperature, however it is still far from the Basin B value after 200 ns at 320K. (c) The ratio of pore radius to its uncertainty rapidly decreases initially and approaches the Basin B value smoothly until they finally overlap at 320K.

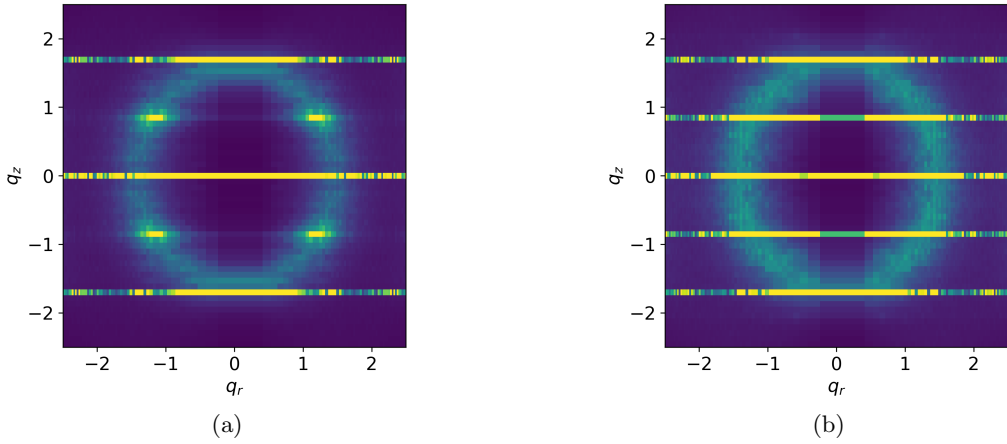


Figure 7: (a) Simulated X-ray diffraction of a sandwiched configuration with restraints placed on aromatic carbons shows all major features present experimental WAXS. Near solid lines at constant z are a result of the highly ordered aromatic rings. (b) Simulated X-ray diffraction of a similarly restrained parallel displaced configuration may also contain all major experimental WAXS features. One can argue that R-spots are not present but it is difficult to distinguish because of its intersection with the solid R-helix line. Longer simulations are necessary to determine which structure is the best match to experiment

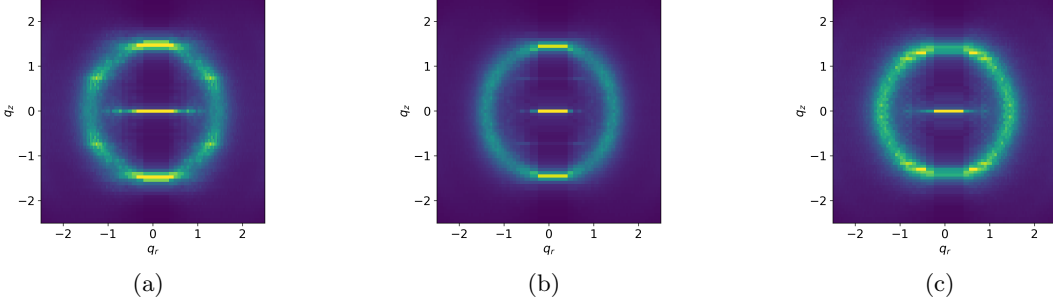


Figure 8: (a) All major features except R-helix are present in XRD patterns resulting from an equilibrated sandwiched configuration in Basin A. R-pi intersects R-alkanes. R-helix faded during equilibration. (b) All major features except R-spots are present in XRD patterns resulting from an equilibrated parallel displaced configuration in Basin A. R-helix exists faintly in the expected location. (c) R-pores and R-alkanes are the only major features present in XRD patterns resulting from an equilibrated disordered phase

suggests that monomers in the parallel-displaced configuration may not give rise to the experimental WAXS pattern seen. Simulated XRD of the sandwiched configuration contains all features except for R-helix. Most notably, R-spots appears in the expected location, which suggests that there is something intrinsic to the sandwiched packing that gives rise to such features. Finally, the disordered structure exhibits R-alkanes and R-pores but R-helix, R-pi and R-spots are not present. Given the evidence, the sandwiched configuration created with layers spaced 3.7 Å apart gives rise to an equilibrated structure closest to experiment.

The spots that appear in the simulated XRD pattern of the sandwiched conformation are a result of the way alkane tails pack together. Previously, the spots in the diffraction pattern had been explained as the product of tilted alkane chains. We measured the tilt angle of the alkane chains and showed that our system equilibrates to an average tilt angle close to zero degrees (Figure 9). To understand the origin of the spots, we determined which atoms gave rise to the feature. By removing atoms from the trajectory and simulating a diffraction pattern, we were able to isolate the cause of the spots to the tails (Figure 10b). Since the tails are mostly flat, we plotted the centroids of the tails and measured the angle between each centroid and its nearest neighbors with respect to the plane of the membrane (Figure ??). The distribution of these angles is consistent with the location of the spots (Figure 10d). We reason that monomer tails stacked closely in the sandwiched conformation are forced to splay apart and pack in between in each other which creates a nearly hexagonal array of packed tails.

Ionic conductivity calculation

The model gives reasonable estimates of ionic conductivity for both phases. Calculated values of ionic conductivity obtained using the Nernst Einstein relation and Collective Diffusion model are compared in Table 2. The two methods agree with each other within error, although the uncertainty obtained using the Collective Diffusion model is much higher. Much longer simulations are needed to lower the uncertainty. This is especially true of the value calculated for Basin B using the collective diffusion model. The simulation was only run for 200 ns. Basin A collective diffusion calculations were generated from a 500 ns simulation. In both cases, our calculated values would benefit from longer simulations. For this reason we will likely only use the Nernst Einstein relation in future calculations of this type. Interestingly, Basin B has a higher ionic conductivity than Basin A. Conductivity is enhanced in Basin B due to a higher sodium ion diffusivity. Transport of sodium is likely facilitated by the homogeneity of Basin B. Sodium ions have less sites to move to in Basin A. Currently there is no experimental evidence of this trend, but it may be the subject of a future study. In both cases, our calculated values for Basin A are higher than the experimental values, as expected. Some of the discrepancy is likely a result of using an imperfect forcefield. However, the real system, although mostly aligned and straight, has a distribution of azimuthal angles, meaning that the pores have a degree of tortuosity which lowers the effective ionic conductivity of the bulk membrane. The ordering from isotropic to mostly aligned mesophases showed an 85 fold increase in ionic conductivity. We would expect additional

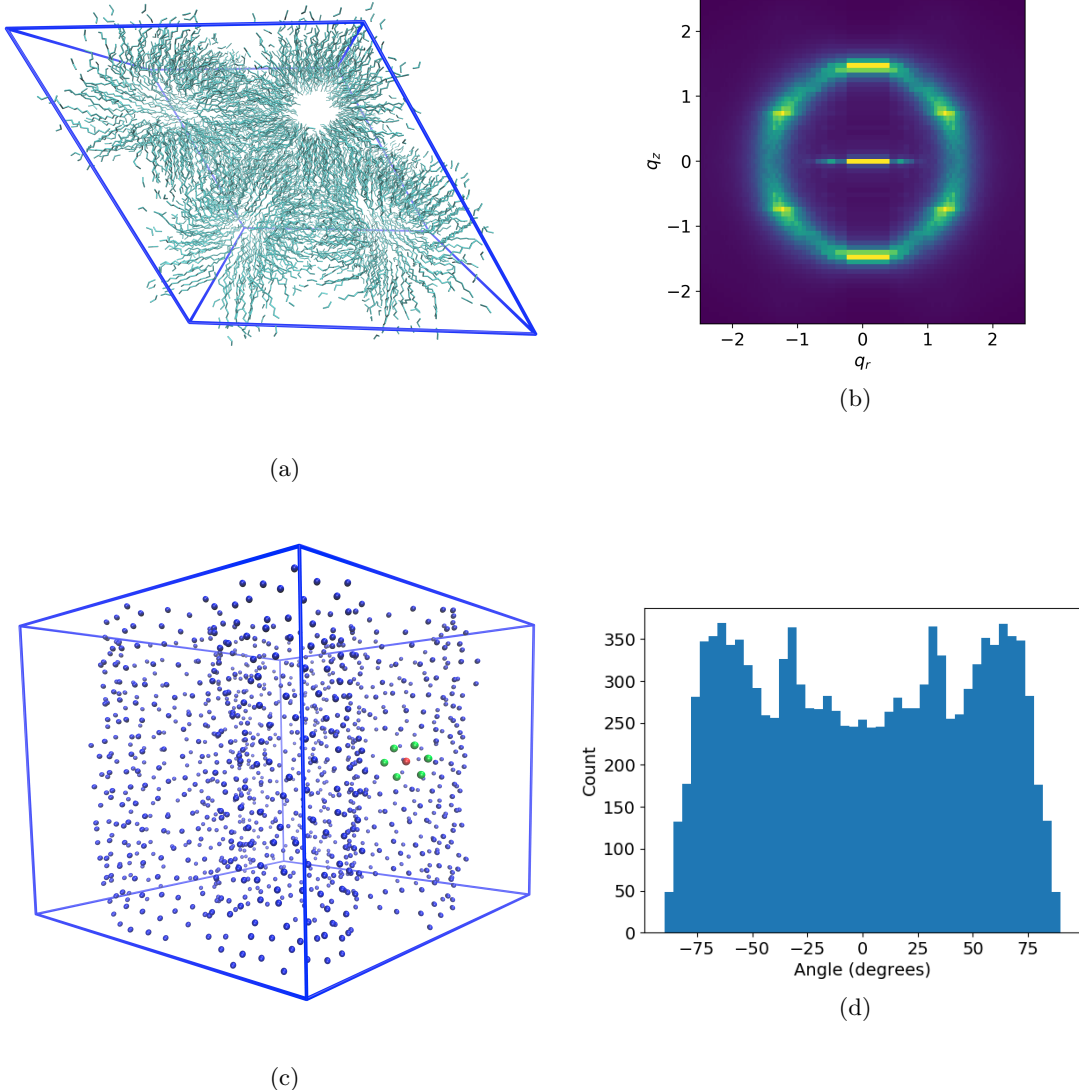


Figure 10: (a) The trajectory can be stripped of all atoms except carbon atoms in monomer tails. (b) Simulated diffraction of the tail-only trajectory still gives rise to R-spots. (c) Finding the center of mass and visualizing their coordinates reveals the hexagonal-like packing of the tails. (d) The distribution created by measuring the angle between each centroid (e.g. red in (c)) and its nearest neighbors (e.g. green in (c)) with respect to the xy plane has distinct spikes near 30° , which is consistent with the location of R-spots

Method	Calculated Ionic Conductivity Sm^{-1}	
	Basin A	Basin B
Nernst Einstein	1.23×10^{-4} (0.01)	1.76×10^{-4} (0.02)
Collective Diffusion	1.40×10^{-4} (0.32)	4.6×10^{-4} (2.4)
Experiment	1.33×10^{-5} (0.10)	—

Table 2: Calculated ionic conductivity using Nernst-Einstein and Collective Diffusion agree within error. Both methods give calculated values of ionic conductivity which are an order of magnitude higher than experimental values

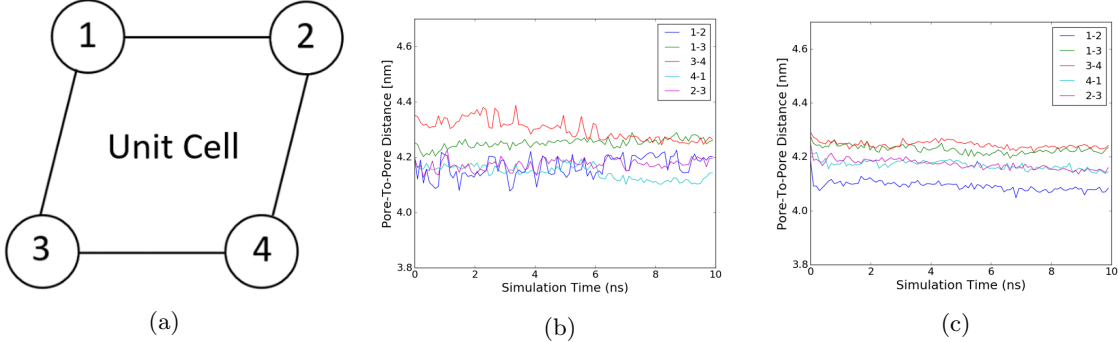


Figure 11: (a) The legends of the plots in (b) and (c) refer to the numbers shown. Each numbered circle represents a pore. Distances are measured along each of the lines shown in addition to the distance from pore 1 to pore 4. (b) The positions of individual pores fluctuate in an uncrosslinked system. (c) The positions of individual pores in the crosslinked system are stable relative to the uncrosslinked system

gains in a perfect system.

Implementation of the crosslinking algorithm

We applied the crosslinking algorithm to an equilibrated structure in Basin B. The procedure will be repeated with Basin A in the near future. The resulting crosslinked structure has an even distribution of crosslinks between monomer tails of the same monomer, monomers stacked on top of each other and monomers in other pores, including across periodic boundaries. The pore spacing shrinks by $\approx 1 \text{ \AA}$ and stays constant under a range of simulation conditions. Figure 11 compares the pore behavior of a system that was a crosslinked and simulated for 10 ns to the pore behavior of the same system taken just before crosslinking and run for 10 ns. Rather than plotting an average pore spacing, each pore-to-pore distance is plotted separately. Visually, one can tell that the crosslinked pores are locked in place. The smaller pore spacing is also apparent by comparing the two plots. The simulations discussed previously have not been crosslinked. Moving forward, the sandwiched system will be crosslinked in Basin A and used for transport studies.

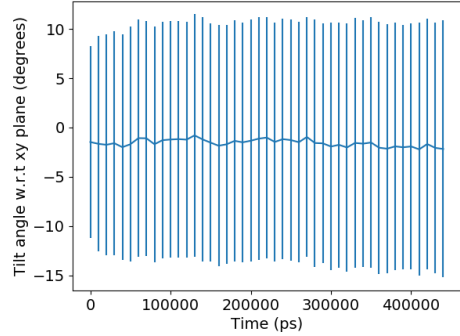


Figure 9: The average angle between alkane chains and the xy plane is nearly zero degrees

Conclusion

In this work, we have illustrated a more detailed picture of the structure of a self-assembled thermotropic liquid crystal membrane using an atomistic molecular model. Using the model we have learned that these liquid crystal monomers prefer to stack in a sandwiched configuration with five monomers in each layer. By a thorough analysis of the membrane structure, we have discovered the existence of two metastable basins that both persist at room temperature. Structurally, Basin A matches closest to experiment, while Basin B has not been seen experimentally. We hypothesize that Basin B will be dominant at higher temperatures. Our model's inability to capture aromatic interactions likely destabilizes Basin A at room temperature and enhances the stability of Basin B. Basin B is likely a part of the transition towards the isotropic phase which exists at high temperatures. This hypothesis will be tested in future work. In addition to structural accuracy, our model's physical properties are consistent with experimental measurements. Ionic conductivity, calculated in two ways, is in reasonable agreement with experiment. The procedure used to create and validate our model can be used to evaluate other liquid crystalline assemblies. Using the design framework and analysis methods applied herein, we have the ability to understand structures of new and unsynthesized nanoporous membranes.

References

- [1] T. Humplik, J. Lee, S. C. OHern, B. A. Fellman, M. A. Baig, S. F. Hassan, M. A. Atieh, F. Rahman, T. Laoui, R. Karnik, and E. N. Wang, “Nanostructured materials for water desalination,” *Nanotechnology*, vol. 22, no. 29, p. 292001, 2011.
- [2] B. Van Der Bruggen, C. Vandecasteele, T. Van Gestel, W. Doyen, and R. Leysen, “A review of pressure-driven membrane processes in wastewater treatment and drinking water production,” *Environmental Progress*, vol. 22, pp. 46–56, Apr. 2003.
- [3] X. Song, Z. Liu, and D. D. Sun, “Nano Gives the Answer: Breaking the Bottleneck of Internal Concentration Polarization with a Nanofiber Composite Forward Osmosis Membrane for a High Water Production Rate,” *Advanced Materials*, vol. 23, pp. 3256–3260, Aug. 2011.
- [4] R. L. McGinnis and M. Elimelech, “Global Challenges in Energy and Water Supply: The Promise of Engineered Osmosis,” *Environmental Science & Technology*, vol. 42, pp. 8625–8629, Dec. 2008.
- [5] J. G. Wijmans and R. W. Baker, “The solution-diffusion model: a review,” *Journal of Membrane Science*, vol. 107, pp. 1–21, Nov. 1995.
- [6] W. R. Bowen and J. S. Welfoot, “Modelling the performance of membrane nanofiltrationcritical assessment and model development,” *Chemical Engineering Science*, vol. 57, pp. 1121–1137, Apr. 2002.
- [7] D. Cohen-Tanugi, L.-C. Lin, and J. Grossman, “Multilayer Nanoporous Graphene Membranes for Water Desalination,” *Nano Letters*, vol. 16, pp. 1027–1033, Jan. 2016.
- [8] K. Hata, D. N. Futaba, K. Mizuno, T. Namai, M. Yumura, and S. Iijima, “Water-Assisted Highly Efficient Synthesis of Impurity-Free Single-Walled Carbon Nanotubes,” *Science*, vol. 306, pp. 1362–1364, Nov. 2004.
- [9] S. Maruyama, E. Einarsson, Y. Murakami, and T. Edamura, “Growth process of vertically aligned single-walled carbon nanotubes,” *Chemical Physics Letters*, vol. 403, pp. 320–323, Feb. 2005.
- [10] S. MURAD, K. ODER, and J. LIN, “Molecular simulation of osmosis, reverse osmosis, and electro-osmosis in aqueous and methanolic electrolyte solutions,” *Molecular Physics*, vol. 95, pp. 401–408, Oct. 1998.
- [11] L. Li, J. Dong, T. M. Nenoff, and R. Lee, “Desalination by reverse osmosis using MFI zeolite membranes,” *Journal of Membrane Science*, vol. 243, pp. 401–404, Nov. 2004.
- [12] X. Feng, M. E. Tousley, M. G. Cowan, B. R. Wiesenauer, S. Nejati, Y. Choo, R. D. Noble, M. Elimelech, D. L. Gin, and C. O.

- Osuji, "Scalable Fabrication of Polymer Membranes with Vertically Aligned 1 nm Pores by Magnetic Field Directed Self-Assembly," *ACS Nano*, vol. 8, pp. 11977–11986, Dec. 2014.
- [13] R. C. Smith, W. M. Fischer, and D. L. Gin, "Ordered Poly(p-phenylenevinylene) Matrix Nanocomposites via Lyotropic Liquid-Crystalline Monomers," *Journal of the American Chemical Society*, vol. 119, no. 17, pp. 4092–4093, 1997.
- [14] M. Zhou, T. J. Kidd, R. D. Noble, and D. L. Gin, "Supported Lyotropic Liquid-Crystal Polymer Membranes: Promising Materials for Molecular-Size-Selective Aqueous Nanofiltration," *Advanced Materials*, vol. 17, pp. 1850–1853, Aug. 2005.
- [15] R. Resel, U. Theissl, C. Gadermaier, E. Zojer, M. Kriechbaum, H. Amenitsch, D. Gin, R. Smith, and G. Leising, "The H₂-phase of the lyotropic liquid crystal sodium 3,4,5-tris(omega-acryloyloxyundecyloxy)benzoate," *Liquid Crystals*, vol. 27, pp. 407–411, Mar. 2000.
- [16] X. Feng, S. Nejati, M. G. Cowan, M. E. Tousley, B. R. Wiesennauer, R. D. Noble, M. Elimelech, D. L. Gin, and C. O. Osuji, "Thin Polymer Films with Continuous Vertically Aligned 1 nm Pores Fabricated by Soft Confinement," *ACS Nano*, vol. 10, pp. 150–158, Jan. 2016.
- [17] R. Resel, G. Leising, P. Markart, M. Kriechbaum, R. Smith, and D. Gin, "Structural properties of polymerised lyotropic liquid crystals phases of 3,4,5-tris(\$mega\$-acryloxyalkoxy)benzoate salts," *Macromolecular Chemistry and Physics*, vol. 201, no. 11, pp. 1128–1133, 2000.
- [18] X. Zhu, M. Scherbina, A. Bakirov, B. Gorzolnik, S. Chvalun, U. Beginn, and M. Moller, "Methacrylated Self-Organizing 2,3,4-Tris(alkoxy)benzenesulfonate: A New Concept Toward Ion-Selective Membranes," *ACS: Chemistry of Materials*, vol. 18, no. 19, pp. 4667–4673, 2006.
- [19] E. Gazit, "A possible role for -stacking in the self-assembly of amyloid fibrils," *The FASEB Journal*, vol. 16, pp. 77–83, Jan. 2002.
- [20] M. O. Sinnokrot, E. F. Valeev, and C. D. Sherrill, "Estimates of the Ab Initio Limit for Interactions: The Benzene Dimer," *Journal of the American Chemical Society*, vol. 124, pp. 10887–10893, Sept. 2002.
- [21] M. P. Waller, A. Robertazzi, J. A. Platts, D. E. Hibbs, and P. A. Williams, "Hybrid density functional theory for -stacking interactions: Application to benzenes, pyridines, and DNA bases," *Journal of Computational Chemistry*, vol. 27, pp. 491–504, Mar. 2006.
- [22] A. L. Ringer, M. O. Sinnokrot, R. P. Lively, and C. D. Sherrill, "The Effect of Multiple Substituents on Sandwich and T-Shaped Interactions," *Chemistry A European Journal*, vol. 12, pp. 3821–3828, May 2006.

- [23] J. Wang, R. M. Wolf, J. W. Caldwell, P. A. Kollman, and D. A. Case, “Development and testing of a general amber force field,” *Journal of Computational Chemistry*, vol. 25, pp. 1157–1174, July 2004.
- [24] J. Wang, W. Wang, P. A. Kollman, and D. A. Case, “Automatic atom type and bond type perception in molecular mechanical calculations,” *Journal of Molecular Graphics and Modelling*, vol. 25, pp. 247–260, Oct. 2006.
- [25] D. Case, R. Betz, W. Botello-Smith, D. Cerutti, T. Cheatham, III, T. Darden, R. Duke, T. Giese, H. Gohlke, A. Goetz, N. Homeyer, S. Izadi, P. Janowski, J. Kaus, A. Kovalenko, T. Lee, S. LeGrand, P. Li, C. Lin, T. Luchko, R. Luo, B. Madej, D. Mermelstein, K. Merz, G. Monard, H. Nguyen, H. Nguyen, I. Omelyan, A. Onufriev, D. Roe, A. Roitberg, C. Sagui, C. Simmerling, J. Swails, R. Walker, J. Wang, R. Wolf, X. Wu, L. Xiao, D. York, and P. Kollman, “AmberTools16,” Apr. 2016.
- [26] H. Bekker, H. J. C. Berendsen, E. J. Dijkstra, S. Achterop, R. van Drunen, D. van der Spoel, A. Sijbers, H. Keegstra, B. Reitsma, and M. K. R. Renardus, “Gromacs: A parallel computer for molecular dynamics simulations,” *Physics Computing*, 1993.
- [27] H. J. C. Berendsen, D. van der Spoel, and R. van Drunen, “GROMACS: A message-passing parallel molecular dynamics implementation,” *Computer Physics Communications*, vol. 91, pp. 43–56, Sept. 1995.
- [28] D. Van Der Spoel, E. Lindahl, B. Hess, G. Groenhof, A. E. Mark, and H. J. C. Berendsen, “GROMACS: Fast, flexible, and free,” *Journal of Computational Chemistry*, vol. 26, pp. 1701–1718, Dec. 2005.
- [29] B. Hess, C. Kutzner, D. van der Spoel, and E. Lindahl, “GROMACS 4: Algorithms for Highly Efficient, Load-Balanced, and Scalable Molecular Simulation,” *Journal of Chemical Theory and Computation*, vol. 4, pp. 435–447, Mar. 2008.
- [30] J. Mondal, M. Mahanthappa, and A. Yethiraj, “Self-Assembly of Gemini Surfactants: A Computer Simulation Study,” *The Journal of Physical Chemistry B*, vol. 117, pp. 4254–4262, Apr. 2013.
- [31] L. Martnez, R. Andrade, E. G. Birgin, and J. M. Martnez, “PACKMOL: A package for building initial configurations for molecular dynamics simulations,” *Journal of Computational Chemistry*, vol. 30, pp. 2157–2164, Oct. 2009.
- [32] A. Einstein, “Investigations on the theory of the brownian movement,” *Dover Publications*, 1956.
- [33] Y. Liu and F. Zhu, “Collective diffusion model for ion conduction through microscopic channels,” *Biophysical Journal*, vol. 104, pp. 368–376, Jan. 2013.